Rare Metal Materials and Engineering
Volume 53, Issue 8, August 2024
Available online at www.rmme.ac.cn

Science Press

Cite this article as: Pu Yunna, Zhao Dewei, Liu Binbin, et al. Microstructure Evolution and Mechanical Properties of Ti-25Ta Alloy Fabricated by Selective Laser Melting and Hot Isostatic Pressing[J]. Rare Metal Materials and Engineering, 2024, 53(08): 2123-2130. DOI: 10.12442/j.issn.1002-185X.20230703.

ARTICLE

Microstructure Evolution and Mechanical Properties of Ti-25Ta Alloy Fabricated by Selective Laser Melting and Hot Isostatic Pressing

Pu Yunna[1], Zhao Dewei[2], Liu Binbin[3], Shi Qi[1], Li Junlei[2], Tan Chong[1], Shen Zhengyan[1], Xie Huanwen[1], Liu Xin[1]

[1] Guangdong Provincial Key Laboratory of Metal Toughening Technology and Application, National Engineering Research Center of Powder Metallurgy of Titanium & Rare Metals, Institute of New Materials, Guangdong Academy of Sciences, Guangzhou 510650, China; [2] Affiliated Zhongshan Hospital of Dalian University, Dalian 116001, China; [3] State Key Laboratory for Advanced Metals and Materials, University of Science and Technology Beijing, Beijing 100083, China

Abstract: Ti-25Ta alloy samples were fabricated by selective laser melting, and the relative density, microstructure, microhardness and tensile properties of the as-built and hot isostatic pressing (HIP)-prepared samples were characterized. Results show that the track width and penetration depth are increased with the increase in laser power, and the surface morphology is improved. The maximum relative density improves from 95.31% to 98.01% after HIP process. Moreover, the microstructure is refined into the lath martensite and cellular grains with the increase in input power. After densification treatment, the subgrain coalescence occurs and high angle grain boundaries are formed. In addition, HIP process stabilizes the microhardness and enhances the tensile strength and elongation.

Key words: Ti-25Ta alloy; selective laser melting; hot isostatic pressing

Metallic biomaterials should possess outstanding mechanical properties, chemical properties, and corrosion resistance[1]. Currently, numerous types of metals have been used in biomedicine according to the desired specification of implants. Compared with stainless steels and cobalt-based alloys, titanium and its alloys possess excellent corrosion resistance, outstanding biocompatibility, and high specific strength[2–3], thereby presenting great potential as the most promising metallic biomaterial. Among them, Ti-6Al-4V alloy is extensively used due to its combination of superior strength, plasticity, toughness, weldability, and corrosion resistance. Nonetheless, the potential neurological disease problems correlated with the release of Al and V ions[4] and the stress-shield effect correlated with the high modulus[5] are considered as the quintessential obstacle. Therefore, the development of the next generation titanium alloys with low elastic modulus and non-metal-related toxicities is of great significance in the field of biomedical industry.

Tantalum (Ta) can promote cell adhesion, proliferation, differentiation, and mineralization in vitro and in vivo[6], therefore being widely used as coating or implants[7–8]. Furthermore, the binary Ti-Ta alloy has gained wide attention due to its excellent mechanical compatibility and biocompatibility. Zhou et al[9] found that the microstructure, dynamic Young's modulus, and tensile properties of the as-cast Ti-Ta alloys strongly depend on the Ta content. It was demonstrated that Ti-30Ta and Ti-70Ta alloys possessed the low modulus of 69 and 67 GPa, respectively. Zhou et al[10] also confirmed that the Ti-25Ta alloy had the lowest elastic modulus of 64 GPa and the highest ratio of strength to

Received date: November 08, 2023
Foundation item: Key Realm R&D Program of Guangdong Province (2018B090904004); Supported by State Key Laboratory of Advanced Metals and Materials (2022-Z16); Key Research Program of Guangzhou (202206040001); International Science and Technology Cooperation Program of Guangdong Province (2022A0505050025); Guangdong Academy of Science Project of Science and Technology Development (2020GDASYL-20200504001, 2022GDASZH-2022010107, 2022GDASZH-2022010109); National Key Research and Development Project (2022YFC2406000)
Corresponding author: Shi Qi, Ph. D., Senior Engineer, Guangdong Provincial Key Laboratory of Metal Toughening Technology and Application, National Engineering Research Center of Powder Metallurgy of Titanium & Rare Metals, Institute of New Materials, Guangdong Academy of Sciences, Guangzhou 510650, P. R. China, E-mail: shiqi@gdinm.com

modulus (7.5×10^{-3}) among Ti-Ta alloys.

Compared with the conventional methods, such as casting and powder metallurgy, which usually have geometry design and forming flexibility restrictions, the rapid development of additive manufacturing provides an alternative technique to fabricate parts with complex geometry or porous structure for the individualized implants[11–14]. Brodie et al[6] reported that Ti-25Ta alloy prepared by selective laser melting (SLM) exhibited enhanced alkaline phosphatase activity and mineralization, therefore improving the osteogenic capacity, compared with Ti-6Al-4V alloy. In Ref. [15 – 16], the possibility to fabricate porous-structured Ti-25Ta parts for load-bearing implant applications with controllable elastic modulus via porosity and unit-cell design by SLM technique was discussed. It is noteworthy that the mixed elemental powder is usually used as the raw material, but it might raise the heterogeneity problem, such as unmelted Ta particles[17].

In this research, dense Ti-25Ta parts were prepared from pre-alloyed powder by SLM and subsequent hot isostatic pressing (HIP) treatments. The influences of laser power input during SLM process on the scanning track, densification behavior, microstructure, and mechanical properties were discussed. The impacts of the subsequent HIP process on the microstructure evolution and mechanical property enhancement were also evaluated.

1 Experiment

The hydrogeninzed and dehydrogenized (HDH) Ti-25Ta powder was spheroidized by radio frequency plasma spheroidization, and the chemical composition of the initial powder is listed in Table 1. Fig. 1 shows that most particles have high sphericity and smooth surface, which implies that the powder is of good flowability and spreadability without internal defects. The particle size distribution in Fig. 1c illustrates that the feedstock basically presents a Gaussian distribution, and the D_{10}, D_{50}, and D_{90} values are 26.2, 43.8, and 72.1 μm, respectively. The components of Ti-25Ta powder were analyzed by X-ray diffraction (XRD). According to XRD pattern in Fig. 1d, the raw Ti-25Ta powder contains two phases, namely α-Ti phase with hexagonal close packed (hcp) structure and β-Ti phase with body-centered cubic (bcc) structure.

Table 1 Chemical composition of raw Ti-25Ta powder (wt%)

Ta	H	O	C	Ti
24.240	0.019	0.160	0.026	Bal.

SLM experiment was performed on EOS M290 machine under high-purity argon atmosphere. Ti-6Al-4V plate was used as the substrate and pre-heated at 100 °C. The laser power was 80, 120, 160, and 200 W. The layer thickness, hatch spacing, and scanning speed were 30 μm, 60 μm, and 500 mm/s, respectively. The schematic diagrams of SLM experiment and as-built samples are shown in Fig. 2. HIP treatment was conducted following SLM process, and the processing parameters were 900 °C/ 150 MPa/2 h.

The nonmetallic impurities (C/H/O) in the raw powder feedstock were detected by the carbon sulfur analyzer (LECO CS600) and oxygen nitrogen analyzer (ON-3000). The particle size distribution was measured by laser particle size analyzer (Microtrac S3500). The relative density was determined according to Archimedes principle. Bulk samples were etched by Kroll's reagent (HF:HNO_3:H_2O=1:2:50) after grinding and polishing. The microstructure was observed by scanning electron microscope (SEM, Carl Zeiss Gemini 300) equipped with electron backscatter diffracto-

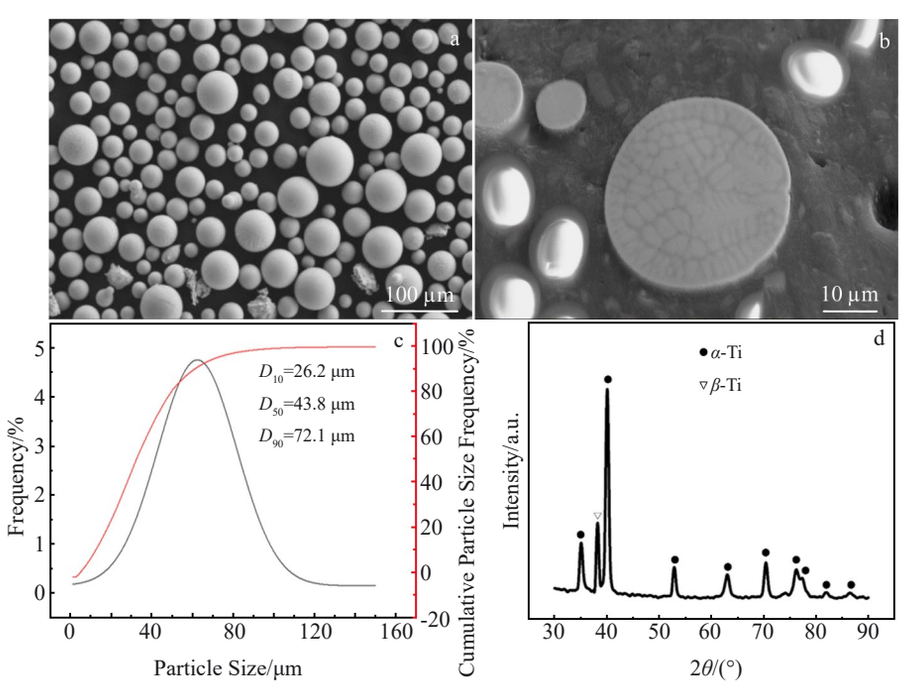

Fig.1 Surface morphology (a), cross-section morphology (b), particle size distribution (c), and XRD pattern (d) of raw Ti-Ta25 powder

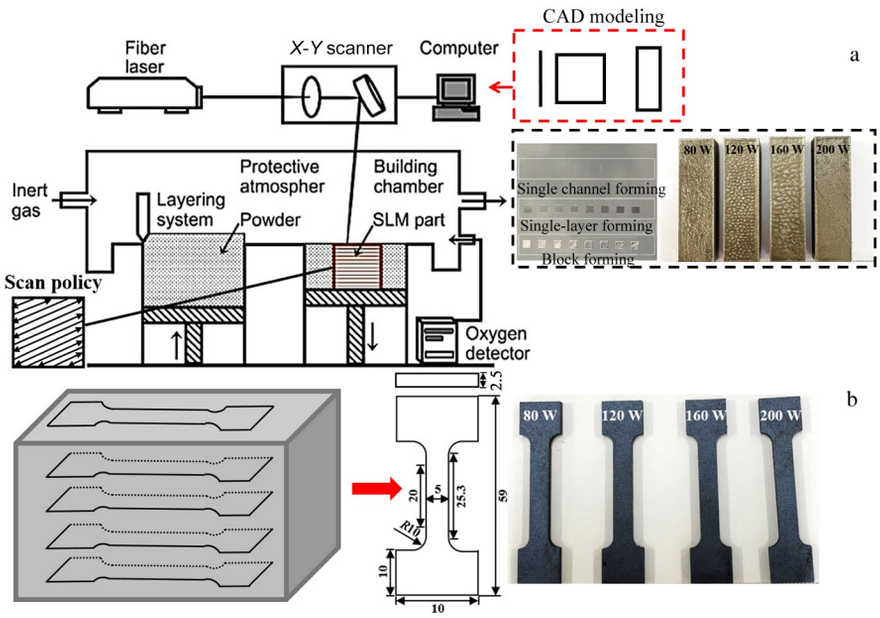

Fig.2 Schematic diagrams of SLM experiment (a) and as-built samples (b)

meter (EBSD, Oxford Symmetry S2). The Vickers microhardness was measured by hardness tester machine (Zwick-Roell Zhu) with load of 0.096 N and dwell time of 10 s. The samples were measured 3 times to obtain the average value. The tensile test was conducted using universal testing machine (Zwick-Roell Z250) with tensile rate of 10 mm/min. The fracture morphology was characterized by SEM.

2 Results and Discussion

2.1 Scanning tracks and densification

During SLM process, the continuous scanning tracks are simultaneously formed with the laser spot movement. Fig.3a–3d show the surface morphologies of single scanning tracks at different laser powers. It can be found that under low laser power of 80 W, the scanning track is uneven, and an irregular

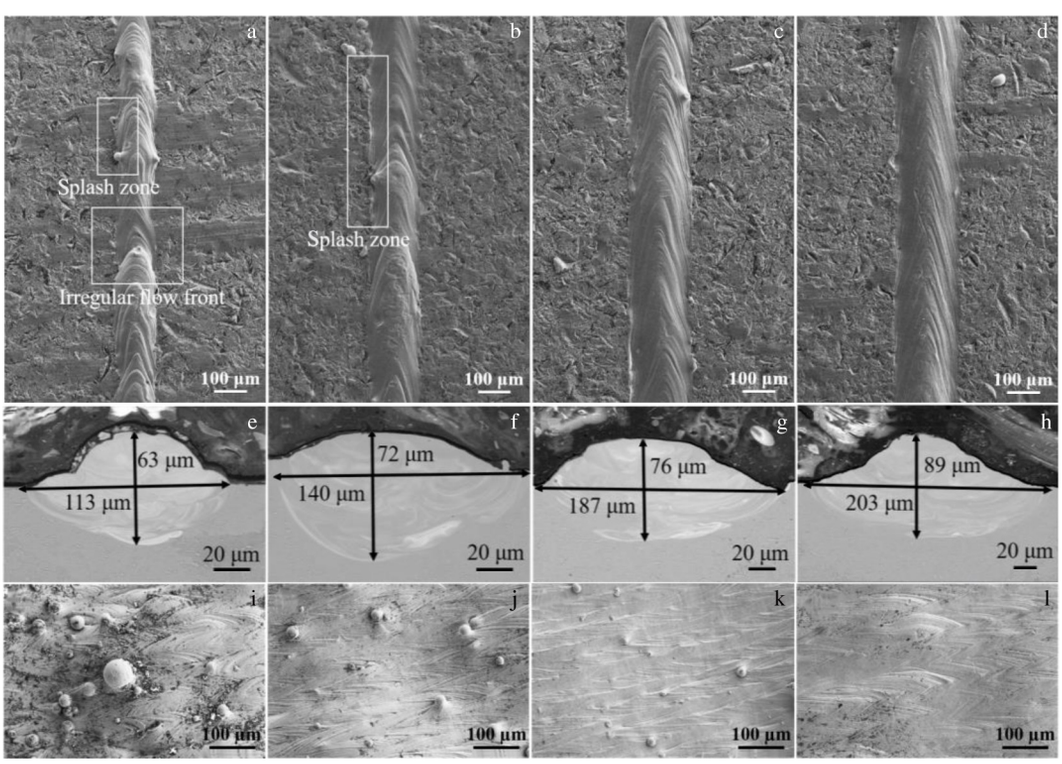

Fig.3 Surface (a–d) and cross-section (e–h) morphologies of single scanning track as well as typical surface morphologies (i–l) of Ti-25Ta samples prepared under different laser powers: (a, e, i) 80 W, (b, f, j) 120 W, (c, g, k) 160 W, and (d, h, l) 200 W

flow front can be observed along the scanning track. This is related to the fact that when the laser power is insufficient, the temperature of the molten pool decreases, and the corresponding viscosity increases, resulting in the poor spreadability and discontinuous track. With the increase in laser power, the wettability of the molten pool is promoted, presenting the even scanning tracks and regular flow fronts[18–20]. With the increase in laser power from 80 W to 200 W, the track width is gradually increased from 104 μm to 198 μm. In addition, the splash zones can be observed in Fig. 3a and 3b. This is because under the lower laser power, unmelted particles are wrapped in the metal flow and adhered to the border of splash zones. With the increase in laser power, unmelted particles disappear, and thus smooth borderlines are obtained.

As shown in Fig. 3e–3h, the height and width of the single scanning tracks are increased with the increase in laser power. The maximum height and width are 203 and 89 μm, respectively, which are obtained under the laser power of 200 W. The height of the scanning track is related to the penetration depth of molten pool under the laser scanning, and the width is related to the spreading of the metallic liquid.

Because the sample is fabricated by layer-related method, the surface quality of each single layer is crucial for the bulk building. The typical surface morphologies of the as-built samples are shown in Fig. 3i–3l. At low laser power of 80 W, rough flow front can be observed and several splashes adhere to the surface (Fig. 3i). With the increase in laser power, the surface morphology has obvious changes, presenting less liquid splashes and smoother appearance.

The relative densities of the as-built and HIPed samples are illustrated in Fig. 4. It is found that the relative density is slightly increased from 94.46% to 95.31% with the increase in laser power from 80 W to 200 W. This is consistent with the scanning track performance, i.e., higher laser power promotes the bonding and filling between adjacent tracks. After HIP treatments, the relative density of the samples can be improved by 2.4%–2.7%, and the maximum value of 98.01% is obtained. This improvement can be attributed to the elimination of pores and microcracks formed during SLM process[21].

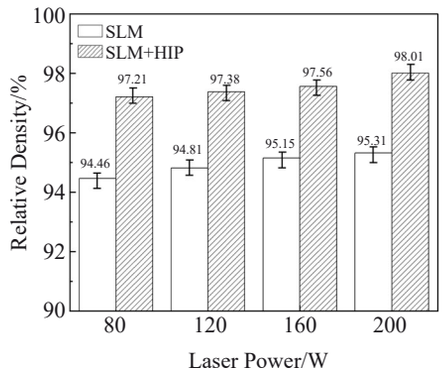

Fig.4 Relative density of built and HIPed Ti-25Ta samples prepared under different laser powers

2.2 Microstructure evolution

The influence of the input laser power on the microstructure of as-built Ti-25Ta samples is shown in Fig. 5. It is obvious that at the lowest energy input (laser power=80 W), a large number of micro-sized pores can be observed, as indicated by the arrows in Fig. 5a. Combined with the analysis of scanning track and surface morphology, it can be speculated that the inadequate spread of the molten pool and the rough interface between two successively built layers may lead to the pore formation. With the increase in laser power, the porosity is decreased, and only a few gaps around the incompletely melted particles can be observed in Fig. 5b. With the increae in laser power, the microstructure evolves from a typical lath martensite with the average width of approximately 0.8 μm (Fig. 5a) to colonies, which consists of parallel and finer acicular structures within the clear prior β grain boundaries. These results are consistent with those in Ref.[16,22].

As shown in Fig. 6, detailed microstructure characterization was analyzed through EBSD for the Ti-25Ta sample fabricated at laser power of 80 W. Combined with the inverse pole figure (IPF) orientation and phase distribution in Fig. 6, it can be distinguished that the Ti-25Ta sample is composed of a large proportion of lath α phase with random orientation and a small quantity of β phase. It is known that Ta has a strong effect on suppressing the β-α phase transformation[23]. How-

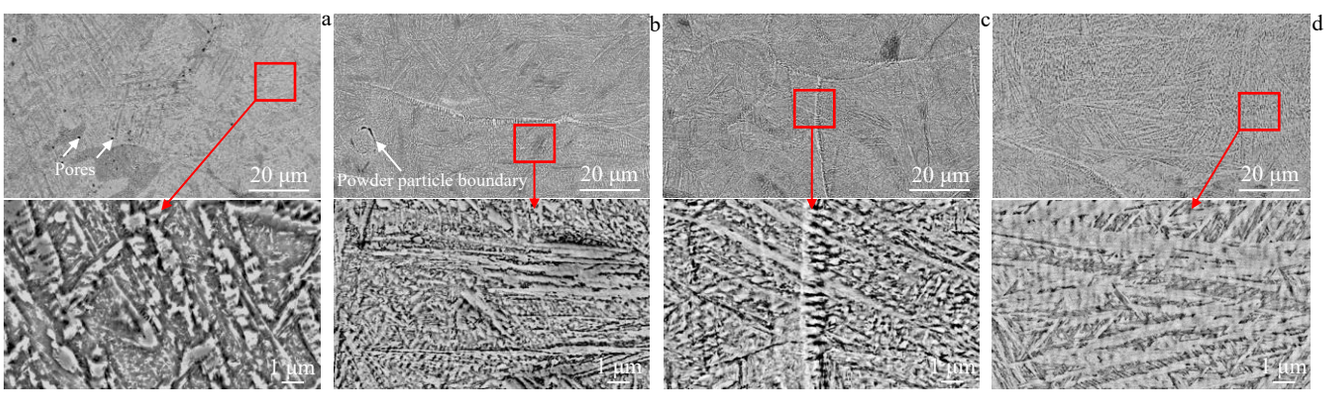

Fig.5 Microstructures of as-built Ti-25Ta samples prepared under different laser powers: (a) 80 W, (b) 120 W, (c) 160 W, and (d) 200 W

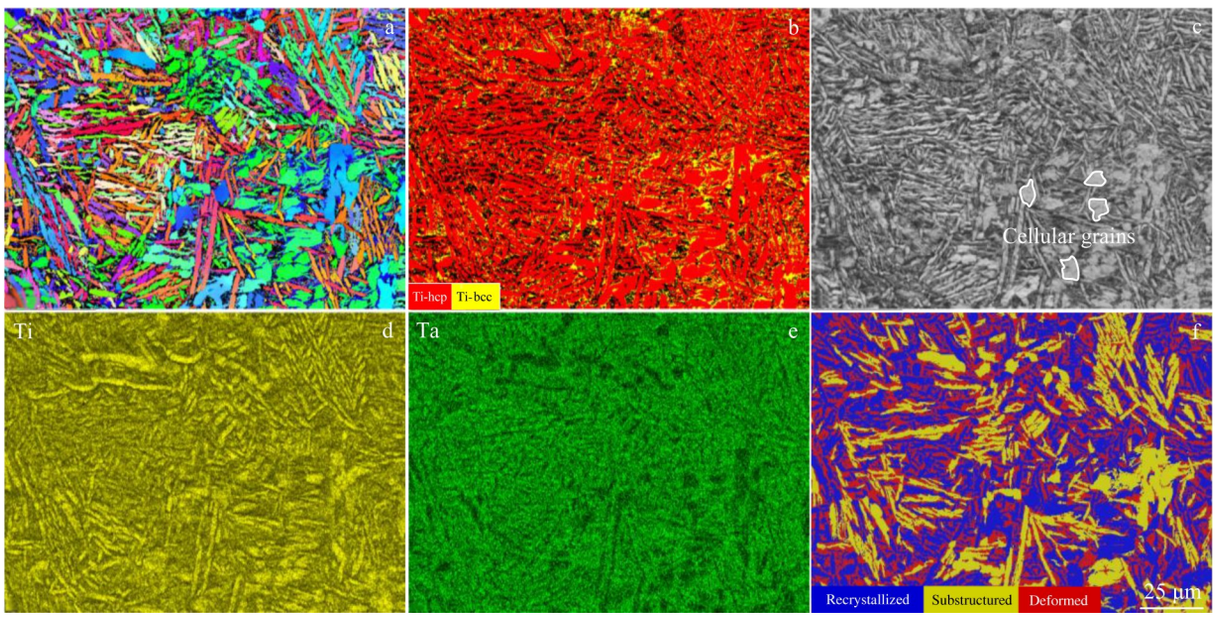

Fig.6 IPF orientation (a), phase distribution (b), band contrast (c), Ti distribution (d), Ta distribution (e), and recrystallized/substructured/deformed region distribution (f) of Ti-25Ta sample prepared under laser power of 80 W

ever, although the 25wt% Ta has equivalent effect as 5wt% molybdenum, it is still insufficient to completely stabilize the β phase[24]. Amongst the laths, a few cellular grains with the size of approximately 6.3 μm can be observed, as indicated by the marked areas in Fig.6c. The element distribution maps of Ti and Ta present homogeneous distributions and no unmelted Ta particles can be found in the sample because of the use of pre-alloyed powder. Micro-segregation can be observed in some grains[25]. The recrystallized (blue), substructured (yellow), and deformed (red) regions represent the areas with misorientation between adjacent grains of less than 2° , between 2° and 15° , and higher than 15° , and their area fractions in the built samples are 43.9%, 24.3%, and 31.8%, respectively. The formation of recrystallization structure may be attributed to the synchronous heat transfer occurring at the subsequent layer under the laser radiation.

Typical SEM microstructures of the Ti-25Ta sample subjected to SLM+HIP treatment show that HIP treatment significantly reduces porosity[26]. Compared with the built sample, the grains basically remain the acicular martensite structure, whose width becomes larger to 1.1 μm. Additionally, the prior β grain boundaries are transformed from cellular shape into smooth structure, as indicated by the arrow in Fig. 7. This may be related to the subgrain recrystallization during HIP process.

EBSD analysis results in Fig. 8 present that HIP process does not dramatically change the microstructure characteristics, α/β phase distribution, and element uniformity. It is noteworthy that the proportions of recrystallized, substructured, and deformed regions are 53.2%, 15.5%, and 31.4%, respectively. Compared with the built sample, the recrystallized region increases, the substructured region decreases, and the deformed region barely changes. It can be inferred that the rearrangement and migration of recrystallization-related grain/subgrain boundaries occur during HIP process, and a large quantity of subgrains coalesce to form grains. Thus, the low angle grain boundaries decrease[27–28]. The measurements mutually corroborate the disappearance of cellular prior β grain boundaries.

2.3 Mechanical properties

The microhardness of the built Ti-25Ta alloy is increased with the increase in laser power, as shown in Fig. 9, and the

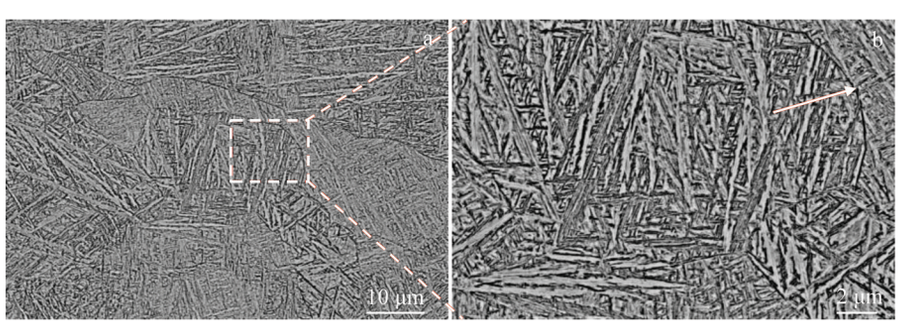

Fig.7 SEM microstructures of Ti-25Ta sample prepared under laser power of 80 W followed by HIP treatment

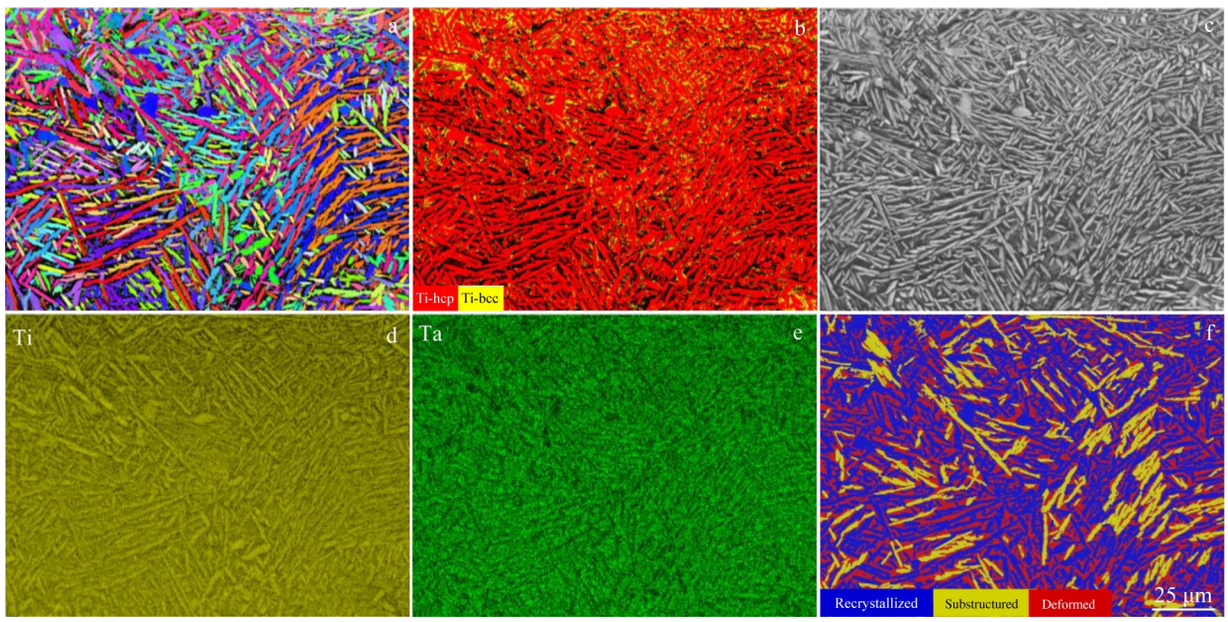

Fig.8 IPF orientation (a), phase distribution (b), band contrast (c), Ti distribution (d), Ta distribution (e), and recrystallized/substructured/deformed region distribution (f) of Ti-25Ta sample prepared under laser power of 80 W followed by HIP treatment

highest $HV_{0.3}$ value of 3608.36±34.30 MPa is obtained for the Ti-25Ta sample fabricated under laser power of 200 W. The variation trend is basically the same as that of relative density. This is because a large number of defects, such as pores, microcracks, and unmelted particles, will degrade the metallurgical bonding and therefore lower the deformation resistance[29–31]. In addition to the internal defect reduction, the refined lamellar structure caused by the increasing laser power also enhances the microhardness.

After HIP treatment, it is observed that the microhardness is relatively stable, regardless of the laser power variation. HIP process has both positive and negative impacts on the microhardness, densification, and microstructure coarsening[32–35]. For the samples fabricated at relatively low laser power, the improvement effect of densification is more obvious, and the significant microhardness enhancement can be observed for the samples prepared at laser power of 80 and 120 W. Nonetheless, these two impacts of HIP treatment are offset by each other for the samples prepared at high temperature because of its relatively higher density and refined microstructure under built condition.

The tensile stress-strain curves of the Ti-25Ta samples prepared under different laser powers before and after HIP treatment are presented in Fig.10, and the test results are listed in Table 2. It can be seen that both strength and elongation are improved with the increase in laser power and addition of HIP treatment. The maximum ultimate tensile strength and elongation are 1182 MPa and 19.5%, respectively. The improvement in the strength and ductility after HIP treatment can be attributed to the coalescence of microvoids[36]. It is clear that the elastic moduli of the built samples are similar (about 67 GPa) regardless of the laser power, whereas the ratio of strength to elastic modulus (1.5×10^{-2}) is much higher than that in Ref.[10].

Fig. 11 shows the fracture surfaces of Ti-25Ta samples prepared under different conditions. It can be seen that the

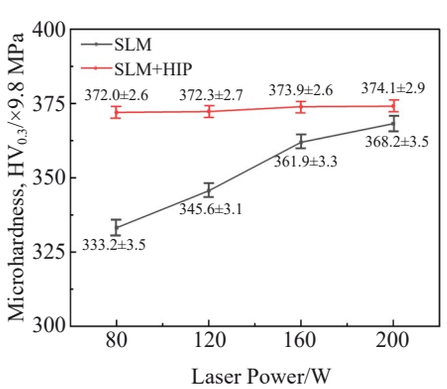

Fig.9 Microhardness of Ti-25Ta samples prepared under different laser powers before and after HIP treatment

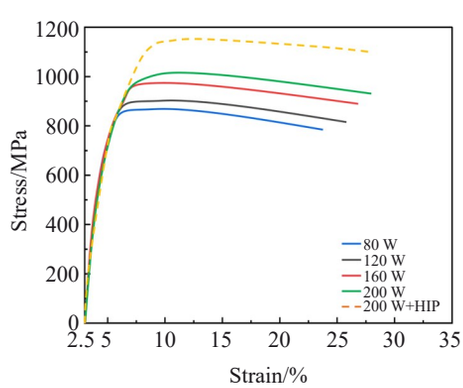

Fig.10 Tensile stress-strain curves of Ti-25Ta samples prepared under different laser powers before and after HIP treatment

Table 2 Tensile properties of Ti-25Ta samples prepared under different laser powers before and after HIP treatment

Sample	Treatment	Laser power/W	Ultimate tensile strength, σ_b/MPa	Yield strength, σ_s/MPa	Elongation, ε/%
1	SLM	80	878	821	13.6
2	SLM	120	904	859	15.0
3	SLM	160	981	896	16.9
4	SLM	200	1035	923	18.8
5	SLM+HIP	200	1182	1139	19.5

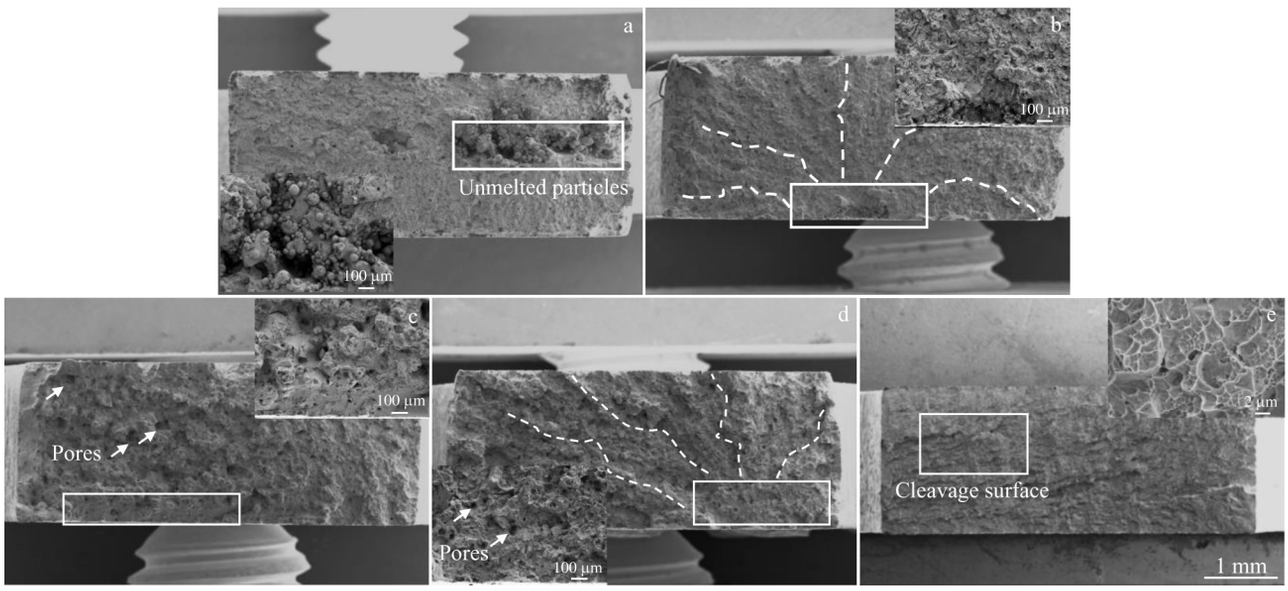

Fig.11 Ti-25Ta samples prepared under different conditions: (a) SLM with laser power of 80 W; (b) SLM with laser power of 120 W; (c) SLM with laser power of 160 W; (d) SLM with laser power of 200 W; (e) SLM with laser power of 200 W+HIP treatment

fracture surface of the sample fabricated under laser power of 80 W (Fig.11a) contains a large number of pores and unmelted particles. These wide-open defects seriously degrade the tensile strength and elongation of alloys[36–37]. When the laser power increases to 120 W, the number of unmelted particles significantly reduces. It is observed that a small number of unmelted particles remain near the surface. With the crack initiation, river-like cleavages originate from the defect region, as shown in Fig.11b. With the further increase in laser power, no obvious unmelted particles can be observed, whereas a large number of pores are formed. These pores act as the initiation positions of microcracks[38]. In addition, the fracture surfaces of the samples prepared under laser power of 160 and 200 W are quite similar and characterized by a mixture of cleavage and dimpled features. After HIP treatment, the fracture morphology is characterized by typical ductile dimples resulting from the defect elimination[39]. As shown in the inset of Fig.11e, a large number of fine and deep dimples can be identified, indicating that the tensile sample suffers uniform plastic deformation.

3 Conclusions

1) With the increase in the laser power, the scanning track and surface morphology of the built Ti-25Ta sample become smooth and continuous. The relative density is increased with the increase in laser power, and a nearly fully dense sample with relative density over 98% is obtained after HIP treatment.

2) The microstructure consisting of lath martensite structure and a small quantity of cellular grains can be obtained in the built sample, and the lath structure is refined with the increase in laser power. HIP treatment leads to the coalescence of sub-grains and grain formation with high angle grain boundaries.

3) The mechanical performance of the built Ti-25Ta alloy is improved with the increase in laser power, which is closely related to the densification behavior of the samples. After HIP process, the microhardness becomes stable and both microhardness and tensile properties are enhanced. Typical ductile fracture characteristics with fine dimples are observed after HIP treatment.

References

1 Geetha M, Singh A K, Asokamani R *et al*. *Progress in Materials Science*[J], 2009, 54(3): 397

2 Karthika P, Olha B, Ming C *et al*. *Materials*[J], 2017, 10(8): 884

3 Niinomi M. *Metallurgical and Materials Transactions A*[J], 2002, 33: 477

4 Rajendran A, Pattanayak D K. *Heliyon*[J], 2022, 8(3): e09122

5 Zhao J C, Tian L Y, Wang S B *et al*. *Journal of Materials Research and Technology*[J], 2023, 26: 5360

6 Brodie E G, Robinson K J, Sigston E *et al*. *ACS Applied BioMaterials*[J], 2021, 4(1): 1003

7 Li X Q, Wang C C, Liang A M. *Surface and Coatings Technology*[J], 2023, 465: 129607

8 Liu B Y, Ma Z J, Li J L *et al*. *Bioactive Materials*[J], 2022, 10: 269

9 Zhou Y L, Niinomi M, Akahori T. *Materials Science and Engineering A*[J], 2004, 371(1–2): 283

10 Zhou Y L, Niinomi M. *Materials Science and Engineering C*[J], 2009, 29(3): 1061

11 Zhao D L, Han C J, Li Y *et al*. *Journal of Alloys and Compounds*[J], 2019, 804: 288

12 Liu G, Zhang X F, Chen X L *et al*. *Materials Science and Engineering R: Reports*[J], 2021, 145: 100596

13 Sing S L, Wiria F E, Yeong W Y. *International Journal of Refractory Metals and Hard Materials*[J], 2018, 77: 120

14 Zhang J, Rynko R, Frenzel J *et al*. *International Journal of Materials Research*[J], 2014, 105(2): 156

15 Soro N, Brodie E G, Abdal-Hay A *et al*. *Materials & Design*[J], 2022, 218: 110688

16 Soro N, Attar H, Brodie E *et al*. *Journal of the Mechanical Behavior of Biomedical Materials*[J], 2019, 97: 149

17 Huang S, Sing S L, De Looze G *et al*. *Journal of the Mechanical Behavior of Biomedical Materials*[J], 2020, 108: 103775

18 Liu B, Fang G, Lei L. *Applied Mathematical Modelling*[J], 2021, 92: 505

19 Gunenthiram V, Peyre P, Schneider M *et al*. *Journal of Materials Processing Technology*[J], 2018, 251: 376

20 Roemer G W R B E, Meijer J. *Lasers in Material Processing*[J], 1997, 3097: 507

21 Patricio M A T, Lustosa C J R, Chaves J A M *et al*. *Journal of Materials Research and Technology*[J], 2021, 14: 210

22 Dobromyslov A V, Dolgikh G V, Dutkevich Y *et al*. *The Physics of Metals and Metallography*[J], 2009, 107: 502

23 Zhou Y L, Niinomi M. *Journal of Alloys and Compounds*[J], 2008, 466(1–2): 535

24 Ehtemam-Haghighi S, Liu Y J, Cao G H *et al*. *Materials Science and Engineering C*[J], 2016, 60: 503

25 Kaplanskii Y Y, Zaitsev A A, Levashov E A *et al*. *Materials Science and Engineering A*[J], 2018, 717: 48

26 Du Plessis A, Macdonald E. *Additive Manufacturing*[J], 2020, 34: 101191

27 Yu H C, Li F Z, Wang Z M *et al*. *International Journal of Fatigue*[J], 2019, 120: 175

28 Yu C L, Huang Z Y, Zhang Z A *et al*. *Journal of Materials Research and Technology*[J], 2022, 18: 29

29 Singh N, Hameed P, Ummethala R *et al*. *Materials Today Advances*[J], 2020, 8: 100097

30 Singh N, Ummethala R, Hameed P *et al*. *Material Design & Processing Communications*[J], 2020, 2(3): e146

31 Jia Q B, Gu D D. *Journal of Alloys and Compounds*[J], 2014, 585: 713

32 Spierings A B, Dawson K, Dumitraschkewitz P *et al*. *Additive Manufacturing*[J], 2018, 20: 173

33 Wang C F, Cai Q, Liu J X *et al*. *Journal of Materials Research and Technology*[J], 2022, 21: 2868

34 Kang L M, Yang C. *Advanced Engineering Materials*[J], 2019, 21(8): 1801359

35 Liu S, Yang W S, Shi X *et al*. *Journal of Alloys and Compounds*[J], 2019, 808: 151160

36 Li W Q, Meng L X, Wang S *et al*. *Materials Science and Engineering A*[J], 2023, 884: 145557

37 Baghi A D, Nafisi S, Hashemi R *et al*. *Journal of Manufacturing Processes*[J], 2021, 68: 1031

38 Liović D, Franulović M, Kamenar E *et al*. *Materials*[J], 2023, 16(12): 4341

39 Ghorbani H R, Kermanpur A, Rezaeian A *et al*. *Journal of Materials Research and Technology*[J], 2023, 24: 5215

选区激光熔化及热等静压制备 Ti-25Ta 合金微观组织和力学性能

蒲芸娜[1]，赵德伟[2]，刘斌斌[3]，施　麒[1]，李军雷[2]，谭　冲[1]，申正焱[1]，谢焕文[1]，刘　辛[1]

(1. 广东省科学院新材料研究所 国家钛及稀有金属粉末冶金工程技术研究中心 广东省金属强韧化技术与应用重点实验室，广东 广州 510650)

(2. 大连大学附属中山医院，辽宁 大连 116001)

(3. 北京科技大学 新金属材料国家重点实验室，北京 100083)

摘　要：采用选区激光熔化技术制备了 Ti-25Ta 合金样品，并对打印件和热等静压样品的相对密度、显微组织、显微硬度和拉伸性能进行了表征。结果表明，随着激光功率的增加，扫描轨迹宽度和深度增加，表面形貌得到改善。经热等静压处理后，样品最大致密度由 95.31% 提高到 98.01%。同时，随着输入功率的增加，晶粒细化为板条马氏体和胞状晶粒。致密化处理后，亚晶粒合并，并形成大角度晶界。热等静压稳定了合金的显微硬度，提高了合金的抗拉伸强度和伸长率。

关键词：Ti-25 合金；选区激光熔化；热等静压

作者简介：蒲芸娜，女，1998 年生，硕士，广东省科学院新材料研究所国家钛及稀有金属粉末冶金工程技术研究中心广东省金属强韧化技术与应用重点实验室，广东 广州 510650，E-mail：1007326159@qq.com